Dielectric tube waveguides with absorptive cladding for broadband, low-dispersion and low loss THz guiding

Bao, Hualong; Nielsen, Kristian; Bang, Ole; Jepsen, Peter Uhd

Published in:
Scientific Reports

Link to article, DOI:
10.1038/srep07620

Publication date:
2015

Document Version
Publisher's PDF, also known as Version of record

SCIENTIFIC REPORTS

OPEN

SUBJECT AREAS:
TERAHERTZ OPTICS
FIBRE OPTICS AND OPTICAL COMMUNICATIONS

Received
15 September 2014

Accepted
3 December 2014

Published
5 January 2015

Correspondence and requests for materials should be addressed to P.U.J. (puje@fotonik.dtu.dk)

Dielectric tube waveguides with absorptive cladding for broadband, low-dispersion and low loss THz guiding

Hualong Bao, Kristian Nielsen, Ole Bang & Peter Uhd Jepsen

DTU Fotonik - Department of Photonics Engineering, Technical University of Denmark, Dk-2800 Kongens Lyngby, Denmark.

Research on terahertz waveguides is experiencing a tremendous growth due to their importance for compact and robust THz systems. However, designing compact, broadband, mechanically stable and environmentally shielded THz waveguides is still a challenge due to high losses of both metals and dielectrics in this frequency range. Here we report on a novel twist on the classical tube waveguide where we deliberately introduce a thick and highly lossy cladding layer. By this we attenuate the field in the cladding and thus prevent interference with the core field. This mechanism breaks the well-known ARROW guiding mechanism, and as a result, extremely broad bandwidth and low dispersion can be achieved with a very simple design. Since the main part of the field propagates inside the air-core, the propagation loss is still kept at a very low level. Simulations, analytical modelling and experiments verify our findings. The proposed THz waveguide is robust, insensitive to external perturbation and easy to handle, and thus the design represents a significant advance of the field of THz dielectric waveguides suitable for the 0.3–1 THz band which in the future will be important for ultrafast wireless communication systems.

Waveguides and functional devices for terahertz (THz) operational frequencies have gained considerable attention in the recent years as they may offer the opportunity to make compact, reliable and flexible THz systems available[1–2]. Numerous metal- and dielectric-based waveguides[2–44] and devices, such as fiber Bragg gratings (FBGs)[45–47] and couplers[48–55], have been studied. However, restistive losses of metals and in particular high absorption of most dielectric materials make design of low loss THz waveguides and devices challenging.

Apart from vacuum, dry air is the most transparent medium in the THz regime. Thus, one viable solution for lowering the propagation loss is to maximize the fraction of the propagating power in dry air.

THz guidance in air has been achieved with low loss and low dispersion in a range of metal waveguides[3–10]. Examples include the parallel-plate waveguide (PPWG)[3], the coaxial waveguide[5], the metal-wire waveguide[6,7,9] and the two-metal-wire waveguide[8–10]. Such waveguides support transverse electromagnetic (TEM) or Sommerfeld wave mode propagation with little modal dispersion and consequently very low group velocity dispersion. At the same time, the loss can be very low in such waveguides due to the large fraction of power that propagates in air. The power absorption coefficient increases with the square root of the frequency and has been observed to be 0.16 cm^{-1} at 1 THz[1], 0.26 cm^{-1} at 1 THz[4], 0.005 cm^{-1} at 1 THz[5] and 0.0062 cm^{-1} at 0.4 THz[6], respectively. The mode of metal-wire waveguide is radially polarized and difficult to be excite (<1% coupling efficiency reported in Ref. 6) with common linearly polarized sources. To address this problem, radially polarized emitters[9] or two-metal-wire waveguides[8] have been demonstrated to increase the excitation efficiency. Two-metal-wire waveguides requires maintaining a constant sub-millimeter distance between the two wires, resulting in a rather fragile structure. The two-metal-wire waveguide can be made easier to handle if a dielectric material[10] is introduced as holder/cladding, resulting in higher loss due to absorption in the dielectric. The losses of such waveguides can be reduced by using dielectric materials with lower absorption. One potential candidate could be high-resistivity silicon, which has a power absorption below 0.01 cm^{-1} throughout the THz range[11]. It would create a new area of high-quality THz interconnects if high-resistivity silicon can shaped or grown for such purpose, but manufacturing costs currently limits such use severely. Recent work has shown relatively undistorted TE1 mode pulse propagation in a PPWG with large plate separation. A power absorption coefficient of less than 0.004 cm^{-1} below 1 THz[4] has been obtained. However, the PPWG suffers to some extent from diffraction losses due to the incomplete transverse confinement of the guided mode[3–4].

Another class of THz waveguides is based purely on low-loss polymers, which can provide properties such as immunity to electromagnetic interference (EMI) and chemical inertness. Several designs for dielectric waveguides with THz radiation propagation in air have already been reported, including sub-wavelength fibers[21-22], porous fibers[23–26], and hollow-core waveguides[27–44]. The guiding mechanism in sub-wavelength fibers is based on total internal reflection. The guided mode field extends far into the surrounding air, thus low loss can be obtained due to the small overlap of the propagating mode and the lossy fiber material. Further reduction of propagation loss can be achieved by inserting a porous structure into the solid core. However, both solid-core and porous-core sub-wavelength fibers are very sensitive to external perturbations and bending, which is a challenge in many applications. Hollow-core waveguides, which normally consist of an air-core and a structured cladding, can alleviate external disturbances as most of the field is guided within the air core region. Several designs based on this kind of structure have been proposed, such as photonic band gap (PBG) type fibers[28–32], Kagome type fibers[33–35] and metal/dielectric tubes[36–43]. For PBG type fibers, the mode is confined within the air core with the help of dielectric reflectors or band-gap reflectors, which prohibit the field from extending into the plane of the PBG reflectors. However, high air filling fraction (photonic bandgap fibers) or high refractive index contrast (Bragg fibers), as well as a strictly periodic cladding structure, are needed to obtain an efficient and broad bandgap[28–30], which are all factors that increase the difficulty of fabrication. Porous-core honeycomb PBG fibers[31–32] can to some extent alleviate such problems of air core fibers, at the expense of introducing more material loss. For Kagome-type fibers[33–35], the cladding can be seen as composed of an array of hollow tubes with different shapes. Unlike the PBG type fibers that guide light by means of a photonic band gap in the cladding, guiding in Kagome-type fibers is based on the inhibited coupling due to the low density of cladding modes and small spatial overlap of cladding modes with core modes. This kind of guiding usually shows abrupt transmission dips within the transmission band caused by the weak but still finite coupling between core modes and cladding modes.

In contrast to hollow-core THz fibers with complex cladding structure discussed above, THz tube waveguides are very simple and normally only consist of a large air-core and a thin dielectric layer[36–40]. The guiding mechanism of the tube waveguides is that of an anti-resonant reflecting optical waveguide (ARROW)[44] with a leaky nature. Low loss has been successfully achieved nearby anti-resonant frequency regions. However, the transmission bandwidth is limited by the spacing of the resonant frequencies, which is proportional to the refractive index and inversely proportional to the cladding thickness. One way to improve the transmission bandwidth is to reduce the cladding thickness. However, a uniformly thin cladding is in practice difficult to fabricate and cleave due to its low mechanical strength. Moreover, tube waveguides with thin walls are fragile and sensitive to external perturbation, as the propagating mode extends significantly outside the cladding. All these disadvantageous aspects could appear as a limiting factor for many practical applications.

Here we present a new class of THz tube waveguides where we deliberately introduce a high-loss, thick cladding, which serves to absorb the propagating field in the cladding and thus prevents it to be reflected back into the core where it otherwise would interfere with the core mode by the normal ARROW mechanism. This results in a very broad transmission band and low dispersion compared to a tube fiber with low-loss cladding. The propagation loss can be kept low due to the high (although not total) reflection that occurs at the core-cladding interface. The supported mode profiles are frequency dependent and show a decreasing mode area thus tighter confinement with increasing frequency. As a result, the loss of this new type of tube waveguides decreases with increasing frequency for all frequencies within the transmission band, in contrast to other common THz waveguides, but similar to the characteristics of capillary waveguides[56]. Moreover, the proposed tube waveguide is robust, insensitive to external perturbations and easy to handle. Finally, bending loss of this tube is also investigated. We use a combination of simulation approaches based on both the Finite Element Method (FEM)[57] and the analytical Fabry-Perot (F-P)[37] model, and experimental characterization with terahertz time-domain spectroscopy (THz-TDS) to verify our findings. Briefly, the F-P model uses the calculated modal index of refraction (the effective index) to calculate the frequency-dependent attenuation of a tube waveguide, based on the total number of bounces of the electric field in the cladding of the material.

Results

Waveguide principle and PMMA characterization. Fig. 1(a) shows the cross section of a PMMA tube waveguide. It has an air core with diameter D surrounded by a cladding layer with thickness t, the cladding layer is made of standard Poly(methyl methacrylate) (PMMA). PMMA is specifically chosen because of its high loss, as compared to for example the low loss cyclic olefin copolymers, such as TOPAS[11] and ZEONEX[14]. The tube waveguide can be described by the ARROW guiding mechanism and its cladding effectively forms an F-P etalon with frequency spacing given by the inverse of its optical thickness. A cross section along the tube waveguide is shown in Fig. 1(b). The light propagates at an angle θ_1, defined by $\sin\theta_1 = n_{\text{eff}}/n_{\text{core}}$, with respect to the normal of the core-cladding interface. Both reflection and transmission occur at the interface between the core and cladding. The reflected part of the light continues to propagate in the core. The part of the light transmitted into the cladding bounces back and forth between the outer and inner interfaces of the cladding, thereby gradually losing its energy to the surrounding and gradually leaking back into the core where it can interfere with the core mode. In the following, we refer to the light that always propagates inside the core, as the first order pulse. The light that experiences a single F-P reflection in the cladding is referred to as the 2nd order pulse, and higher-order reflections from the cladding that experience n times F-P reflection is defined as the pulse of order (n-1).

In order to make a precise and quantitative comparison between experiment and simulation, the bulk dielectric properties (absorption coefficient and refractive index) of PMMA are characterized via THz-TDS[1] using a disk with a thickness of 1.02 mm. The frequency-dependent absorption coefficient and index of refraction are shown in Fig. 1(c). We observe a monotonically increasing absorption coefficient and monotonically decreasing index of refraction with increasing frequency. For the purpose of numerical modelling, a simple polynomial fits to the experimental data (dashed curves in Fig. 1(c) with fit parameters indicated in the caption) are used for representation of the dielectric properties. As can be seen, the material loss of PMMA is significant (approximately 60 dB/cm at 1 THz).

Simulation of straight tube waveguides. We now investigate the transmission properties of straight THz tubes. Our numerical results are based on two methods. We find the effective index of the fundamental mode and the transmission spectrum using the Finite Element (FEM) method and the overlap of the mode with the lossy material (see methods). Correspondingly, we also simulated the transmission properties of the THz tubes using the F-P model[37] and the effective index n_{eff} found from the FEM modelling. Results obtained from the two methods agree well with each other.

Following Lai *et al.*[37], for each polarization component (TE and TM) of the fundamental, hybrid waveguide mode, the F-P model uses the reflection coefficient from the cladding,

$$R = \left| r_{12} - \frac{t_{12} r_{23} t_{21} e^{i2\omega n_2 t \cos\theta_2 / c} e^{-\alpha_2 t/\cos\theta_2}}{1 - r_{23} t_{21} e^{i2\omega n_2 t \cos\theta_2 / c} e^{-\alpha_2 t/\cos\theta_2}} \right|^2, \qquad (1)$$

where ω is the angular frequency, t_{12}, r_{23}, t_{21} are the standard complex-valued Fresnel coefficients for transmission from air core (med-

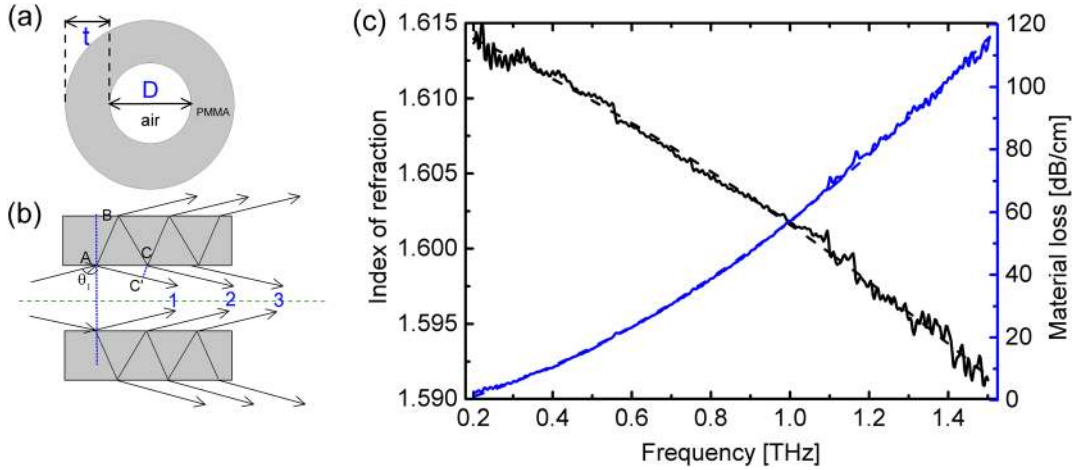

Figure 1 | Profiles of the (a) PMMA tube waveguide and (b) F-P etalon. (c) Refractive index (black curve) and material loss (blue curve) of the PMMA polymer experimentally measured on a disk with thickness of 1.02 mm. Dashed curves are a phenomenological quadratic fits to refractive index ($n(\nu) = -0.0036\nu^2 - 0.0111\nu + 1.6163$) and loss ($\alpha(\nu) = 35.4973\nu^2 + 27.9105\nu - 5.7586$), respectively, used in the simulations.

ium 1) to cladding (medium 2), reflection at the outer interface of the cladding (medium 3 is the surrounding air), and transmission back into the air core, respectively, n_2 and α_2 are the bulk refractive index and absorption coefficient of the cladding, respectively (see Fig. 1c), $\sin\theta_2 = (1/n_2)\sin\theta_1$, and the incident angle, defined from the effective index, is $\theta_1 = \sin^{-1}(n_{eff})$ for an air core fiber ($n_1 = 1$). The effective loss is then calculated as

$$\alpha = -\frac{\ln R}{D\tan\theta_1}\ . \qquad (2)$$

The total loss is calculated as the average of the TE and TM losses. All the loss coefficients mentioned in this paper are defined in terms of power.

In order to demonstrate the effect of cladding material loss on the THz tube transmission, Fig. 2(a) shows transmission loss of the fundamental mode for various values of cladding material absorption. Specifically, we numerically vary the cladding material loss (the imaginary part of the refractive index) while keeping the real part of the refractive index constant. As can be seen in Fig. 2(a), the transmission loss maxima and minima positions are determined mainly by the real part of the refractive index of the cladding through the relation

$$f_m = \frac{mc}{2t\sqrt{n_2^2 - 1}}\ , \qquad (3)$$

and remain almost constant, whereas the overall oscillation amplitude decreases with increasing material loss of the cladding. The F-P model explains this behavior in physics terms. The bouncing cladding field passes through the more lossy cladding material and thus less power is transmitted back to the core to interfere with the direct transmitted field. Figure 2(b) shows three examples of the calculated effective index of the tube from Fig. 2(a), and it can be seen that the absolute value of the slope of the effective index becomes smaller with increasing cladding loss, especially in the vicinity of the resonant loss maxima. Consequently, the corresponding group velocity dispersion (GVD), shown in Fig. 2(d), becomes much smaller with increasing cladding loss. Particularly, extremely low dispersion over the full frequency range can be obtained for a highly absorptive cladding material, effectively eliminating the field propagating through the cladding. The tube dimensions in Fig. 2(a), (b) and (d) are constant with core diameter $D = 4$ mm and cladding thickness $t = 1.29$ mm.

Alternatively, a similar effect can also be achieved by increasing the thickness of the lossy cladding. Figure 2(c) shows the transmission loss of the tube with three different cladding thicknesses, together with the calculated loss for an infinite cladding. In addition to the trivial observation that the loss maxima and minima shift toward lower frequencies with increasing cladding thickness (see Eq. (3)), the oscillation amplitudes display the same trend as the results shown in Fig. 2(a) and become significantly smaller.

Experimental characterization of straight tube waveguides. We perform transmission measurements on straight segments of PMMA tube waveguides using a commercial fiber-coupled THz-TDS system (see Methods). We label the tubes with three different cladding thicknesses $t = 1.29$, 1.97, 2.95 mm as tube 1, 2 and 3, respectively. Measurements are performed on tubes with different lengths (10, 20, 30, 40 cm for tube 1 and 2, and 20, 30, 40 cm for tube 3).

Figures 3(a–c) show the temporal traces of the THz pulses guided through three PMMA tubes with the same air core size ($D = 4$ mm) and different cladding thicknesses $t = 1.29$, 1.97, 2.95 mm. Several pulses are visible in the temporal traces for each tube, corresponding to different orders of the pulses reflected in the cladding. For each tube with different lengths, the temporal delay between adjacent orders is constant, with a time difference proportional to the cladding thickness. This behavior is attributed to the same transmitted path difference between the adjacent orders of pulses in the cladding, which can be expressed as $\delta L = AB + BC - AC' = 2n_2 t\cos\theta_2$ (see Fig. 1(b)). The time delay between the first and second-order pulses in tube 1, 2 and 3, indicated with blue arrows in Figs. 3(a), (b) and (c), are 11.8 ps, 17.6 ps and 26.0 ps, respectively, in agreement with the theoretical value $\Delta t = 2n_2 t\cos\theta_2/c$, which is constant within less than 0.2 ps in the frequency range considered here due to the low dispersion of the refractive index of PMMA. Figures 3(d), (e), and (f) show the corresponding propagation loss of the three tubes. Symbols represent the average value of the experimentally determined loss, based on several measurements on each tube with different lengths. The error bars indicate the standard deviation of the measurements. The simulated losses, based on the FEM simulation (blue circles + line) and the F-P model (black crosses), are shown for direct, quantitative comparison. Within the frequency range from 0.3 to 0.85 THz we find a very close agreement between experiment and simulation, except at the loss maxima where the experimental noise is significant due to low transmitted signal strength[57]. The slight deviation between experiment and simulation at the highest frequencies above 0.9 THz is in part caused by low signal-to-noise ratio in the experiments, but may also be caused by reduced coupling efficiency from the reference tube to the measured tubes at high frequencies. As predicted by

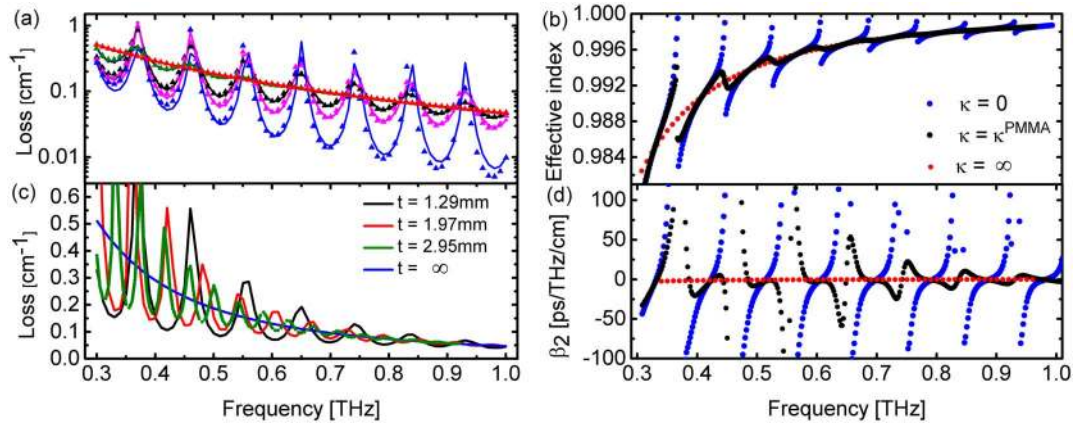

Figure 2 | (a) Simulated propagation loss of the fundamental core mode with constant real part of index of refraction and different loss values κ/κ^{PMMA} (0 – blue; 1/2 – magenta; 1 – black; 4 – olive; ∞ - red). Lines and symbols represent FEM simulation and F-P model, respectively. (b) Calculated effective index of the fundamental mode for the tube with three different loss values κ/κ^{PMMA}. (c) Simulated propagation loss of the fundamental core mode with different cladding thicknesses t and constant core diameter. (d) Calculated group velocity dispersion for the effective indices in (b). Core diameter of all tubes is $D = 4$ mm.

simulations, the experimental results clearly show that the oscillation amplitudes decrease with increasing cladding thickness. For the 2.95-mm thick cladding, the F-P oscillations in the loss spectrum are almost completely suppressed, resulting in a smooth loss curve very close to the simulated loss for an infinite cladding. However, the outer diameter of this waveguide is 9.9 mm, which for some practical purposes may be too bulky.

As an alternative method, the cladding fields can be further suppressed by adding a thin, strongly absorbing layer to the outside of a tube with a thinner cladding. To investigate this idea, we performed an experiment where a thin layer of liquid water was added around the thinnest tube waveguide. Water has a very strong absorption in the THz range ($\alpha \approx 255$ cm^{-1} at 1 THz) and a refractive index matched reasonably well with the PMMA cladding ($n \approx 2.05$ at 1 THz)[58,59] for high transmission of the THz field. These properties make a water layer around the tube a close experimental analog to perfectly absorbing layers in simulations, and thus the water layer should mimic an infinite cladding. In addition to the trivial index-matching properties, the introduction of a high-index, absorptive layer outside the cladding introduces a sign reversal of the reflection coefficient between the TE- and TM components of the THz field, leading to effective cancellation of the F-P oscillations in the fundamental waveguide mode which is a hybrid between the TE and TM modes. For these reasons we therefore repeat the transmission

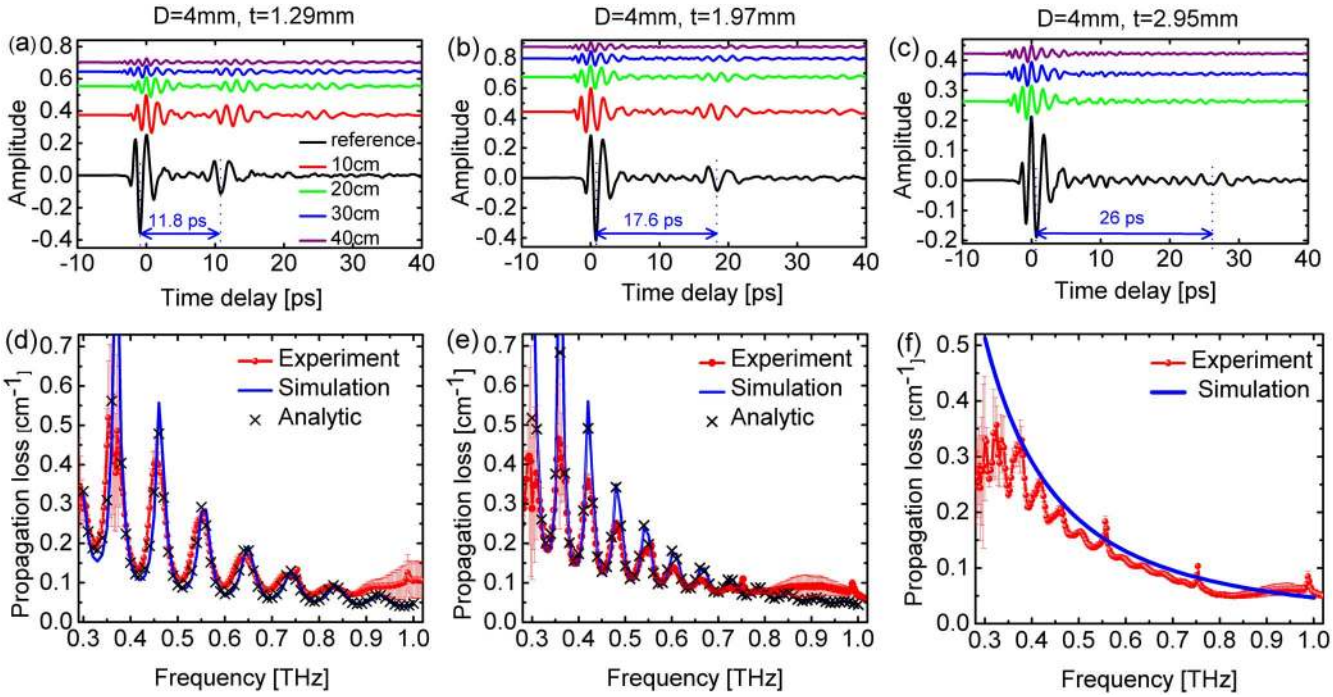

Figure 3 | (a) (b) (c) Measured time-domain THz signals, and (d) (e) (f) propagation loss averaged over the different propagation lengths of three PMMA tubes ($D = 4$ mm) with various cladding thicknesses t. For tube 1 ($t = 1.29$ mm) and tube 2 ($t = 1.97$ mm), using transmission through a 5 cm tube as reference. For tube 3, the transmitted THz signal through 10 cm tube is used as reference. Blue arrows indicate the time delay between the first and second order pulses of each tube. Red error bars in (d) (e) (f) represent the standard deviation between several scans of each tube with different lengths. The blue curve represents FEM simulations, and black crosses represent the analytic F-P model.

experiment on tube 1 with lengths 20 and 40 cm and with a 1.7-mm thick water layer surrounding the tube external surface. The temporal scans of the guided THz pulses in this situation are shown in Fig. 4(a) and they show a prominent suppression of higher-order pulses. The suppression increases with pulse order due to the absorption at each of the multiple reflections at the outer surface of the cladding. In contrast to this behavior we observe that the main pulse, propagating in the core of the tube, is virtually uninfluenced by the added absorptive layer surrounding the cladding. Figure 4(b) shows the measured propagation loss for the two tube lengths with and without water jacket, together with the result of an F-P calculation using the dielectric function of water. We see a good agreement between the measurements and the calculations.

Further insight is obtained by performing a short-time Fourier transform (STFT) of the time-domain traces of 40 cm tube without and with water around the tube external surface, resulting in the spectrograms shown in Fig. 4(c) and (d), respectively. In Fig. 4(c), both the high and low frequency edges of each subsequent higher-order pulse shift toward progressively lower frequencies. The high-order pulses experience longer interaction with the lossy cladding material, resulting in increased loss especially at the higher frequencies. The red-shift of the low-frequency edge of the higher-order pulses is due to high coupling from the core to the cladding, combined with relatively low propagation loss in the cladding material at the lowest frequencies. Again it is observed that after adding water, the main pulse is virtually unaffected while strong attenuation occurs for high order pulses.

Effective index and group velocity dispersion. The frequency-dependent phase and effective index information are determined by the measured data from THz-TDS measurements (see Methods). The simulated (black curve) and experimental (blue dash) effective index for tube 1 without and with water around the cladding are shown in Fig. 5(a) and Fig. 5(b), respectively. The experimentally determined effective index in Fig. 5(a) is obtained by taking the average of the four individual measurements of the index on different lengths of tube 1 (without water around the cladding), and in Fig. 5(b) is the average of the two individual measurements of the index on different lengths of tube 1 (with water around cladding). We find excellent agreement between simulation and experimental results.

The group velocity dispersion (GVD), $\beta_2 = (v\partial^2 n_{eff}/\partial v^2 + 2\partial n_{eff}/\partial v)/2\pi c$[11], is obtained from the experimental effective index for tube 1 without and with water around the tube external surface. The results are also shown as red symbols in Fig. 5(a) and (b), respectively. Since the calculation of β_2 involves the second derivative of the effective index, the calculated results are sensitive to experimental noise, and thus the GVD data shown here are averages over result for tubes with different lengths, and a running average of 5 data points has been applied. The GVD data from experiments follows the pattern of the simulated values (black symbols). We observe that much lower GVD values can be obtained by adding water around the tube external surface, with only slight deviations from the ideal simulation scenario with an infinite cladding, mainly due to the incomplete absorption of the second and third order pulses in the cladding.

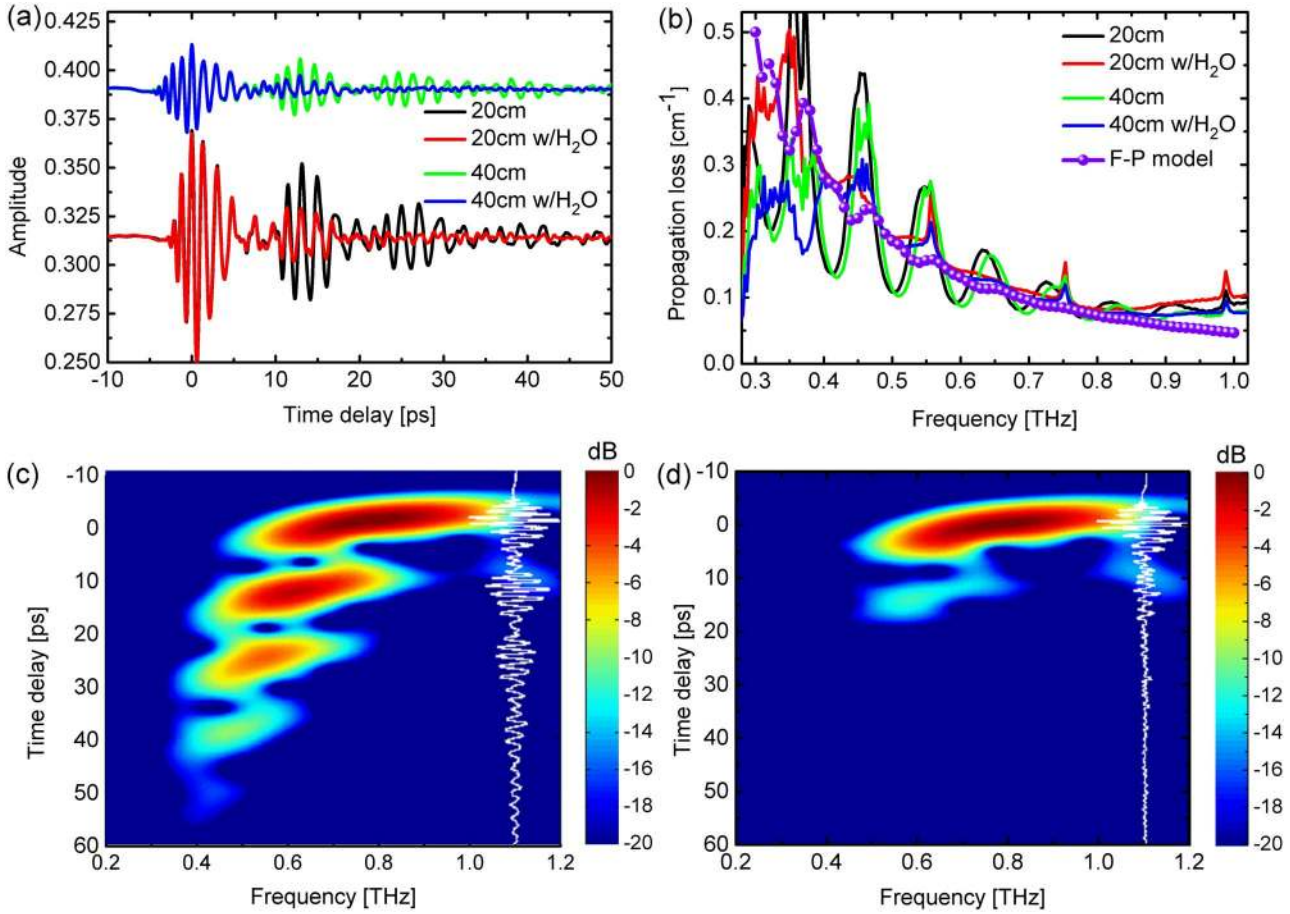

Figure 4 | Measured (a) transmitted pulses and (b) propagation loss for 20 and 40 cm tubes (using transmission through 5 cm tube as reference) with and without water around the tube surface. (c) and (d) show spectrograms (short-time Fourier transforms) of the time traces through 40 cm tube without and with water around the tube surface, respectively, with overlaid time traces of the transmitted pulses.

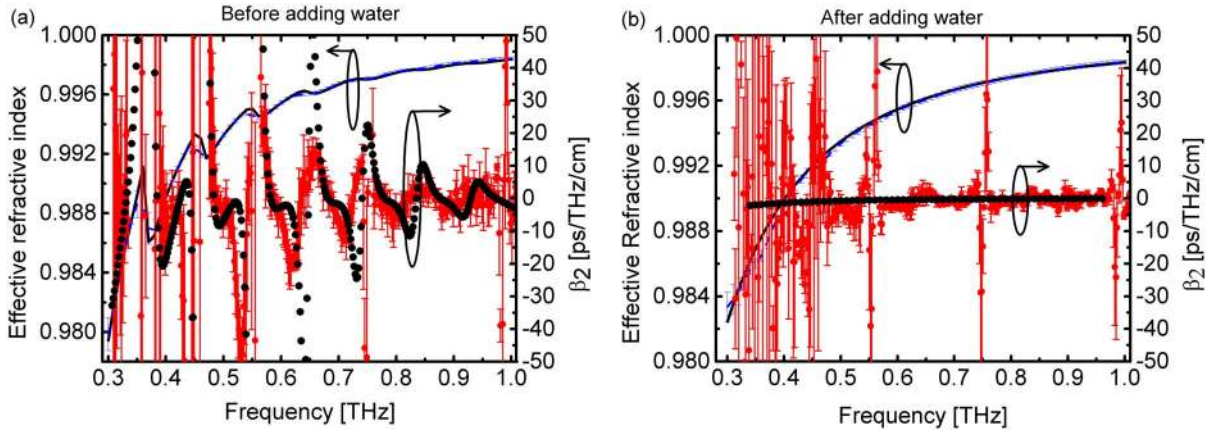

Figure 5 | Simulated (symbols) and measured (curves) effective refractive index and GVD parameter β_2 of tube 1 (a) before and (b) after adding water around the surface. The measured indices in (a) and (b) are the average indices of four different lengths of the tube (before adding water) and two different lengths of the tube (after adding water) and β_2 is the average value of the running average of 5 frequency data points for each length of tube.

Bend loss. Another important parameter associated with THz waveguides is bending loss. The numerical analysis of the bending is performed by employing an equivalent index profile[60] given by $n'(x, y) = n(x, y)e^{x}/R_{bend}$. Here $n(x, y)$ is the index profile of the straight tube waveguide and R_{bend} is the bend radius. In the following, X represents the bending direction. Figures 6(a) and (b) show the geometry and refractive index profile, respectively, of the bent tube. Figures 6(c) and (d) show the simulated transmission loss of tube 1 using the same value for the real part of the refractive index but three different values for the imaginary part ($\kappa = 0$, $\kappa = \kappa^{PMMA}$, and infinite cladding) at three different bending radii ($R_{bend} = \infty$, $R_{bend} = 30$ cm, $R_{bend} = 10$ cm, respectively) and with polarizations perpendicular (Fig. 6(c)) and parallel (Fig. 6(d)) to the bend direction. The general trend is the expected behavior that the bend loss increases with decreasing bend radius. We also see that the frequency positions of loss minima and maxima are the same for the tubes with and without bend loss, and that the loss minima and maxima shift towards lower frequencies as the bend radius is decreased, due to the increased effective cladding thickness after bending. Losses are higher for the parallel polarization than for the perpendicular one, with the higher frequencies being more sensitive to bending than the lower frequencies. Similar to the straight tube transmission loss, the oscillatory features in the bend loss spectrum can also be suppressed if perfectly matched boundary conditions are applied to the outer surface of the cladding, thereby mimicking an infinite cladding. Figure 6(e) shows the intensity profiles of the fundamental mode at 0.740 and 0.805 THz, corresponding to resonant (low loss) and anti-resonant (high loss) frequencies for the straight tube 1, respectively, for straight and bent (R_{bend} = 10 cm) tubes at two polarizations, and with and without inclusion

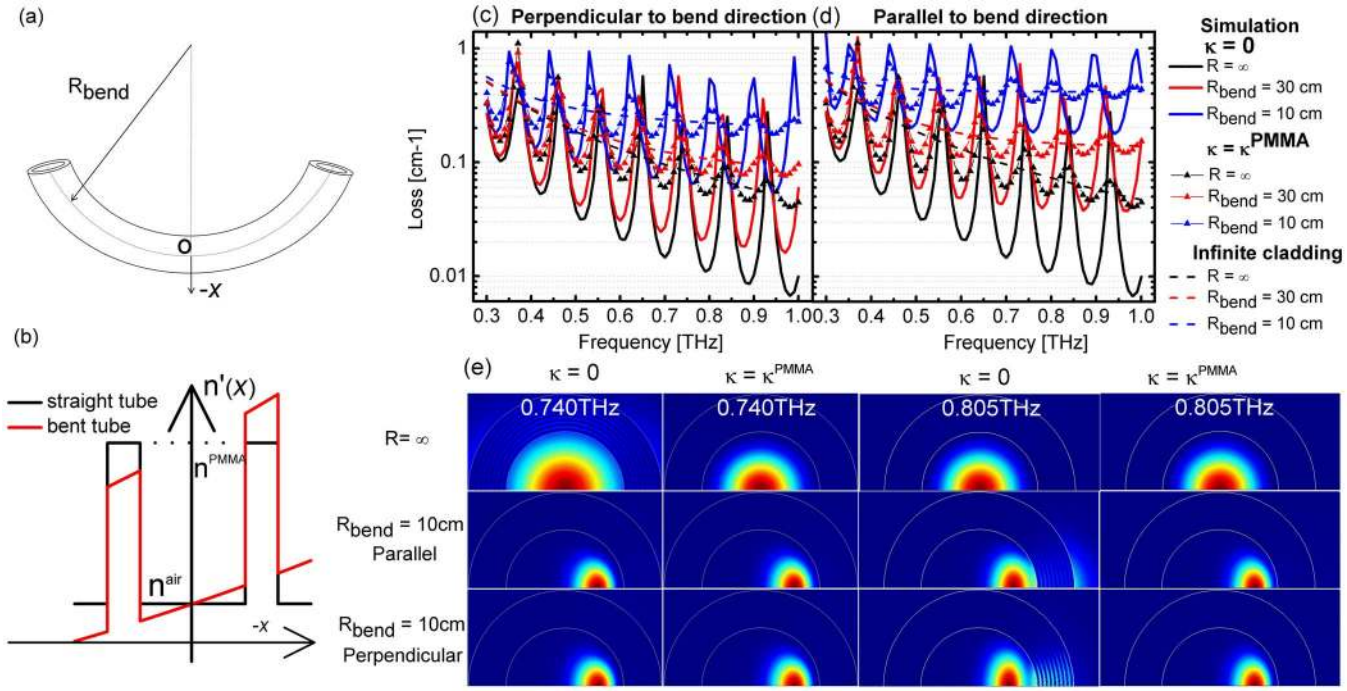

Figure 6 | (a) Geometry and (b) effective refractive index profile of the bent tube. Simulation of propagation loss of tubes (ID = 4 mm, OD = 6.58 mm) with different bending radii for two polarizations (perpendicular (c) and parallel (d) to bend direction) at various values of κ. (e) Calculated intensity distribution of fundamental mode of straight tube and bent tube for the tube with two different loss values for the two polarizations.

of loss. To illustrate the phenomenon of the shift of the maxima and minima of the loss curve, we focus on the simulation without cladding loss, as the visual difference between the intensity distributions for the resonant and anti-resonant cases is most clear in this case. The sub-figures in first and third columns of Fig. 6(e) show that when the tube is bent, the resonance (0.740 THz) of the straight tube experiences a shift towards the anti-resonance frequency region, and the anti-resonance (0.805 THz) becomes a resonant frequency region. The simulations with cladding loss included show that the guided intensity becomes more concentrated in the tube core, thereby reducing the cladding interference behavior and thus resulting in a less pronounced difference in the power distribution between the resonance and anti-resonance case.

Figures 7(a) and (b) present the experimental temporal scans of guided THz pulses through three tubes with different bending radii ($R_{bend} = \infty$, $R_{bend} = 30$ cm, $R_{bend} = 10$ cm, respectively) and with polarizations parallel and perpendicular to the bending direction, respectively. Figures 7(c) and (d) show the bend losses, calculated as the ratio of the transmitted spectrum through the bent and the straight tube. The solid curves are experimental results for the two polarizations. Together with the experimental results we show the simulated bend losses (solid dots) and in general see excellent agreement. The bend losses are negative at some frequencies. This is because the maxima and minima of the loss curves shift slightly with bend radius, as discussed above, leading to oscillations in the bend loss spectra.

Conclusion. We have numerically and experimentally demonstrated a tube waveguide, which guides THz pulses with low loss (0.05–0.5 cm^{-1}) and low dispersion ($|\beta_2| < 10$ ps/THz/cm) in the 0.3–1 THz range, with a bandwidth much larger than a classical ARROW waveguide. The smooth transmission profile and the associated low dispersion is obtained by deliberately introducing material loss to the cladding material, thus efficiently removing the interfering fields that bounce through the cladding and back into the core in a traditional low-loss ARROW tube waveguide. We demonstrate that adding a thin layer of a suitable absorber, here exemplified with water, the dispersion can be even further reduced ($|\beta_2| < 1$ ps/THz/cm in the 0.3–1 THz range), without increasing the overall loss. The absorptive cladding is also effective for reducing the bend loss of the fiber, which remains below 0.2 cm^{-1} for s-polarized light even for tight bending radii down to 10 cm. PMMA tubes of the required dimensions are directly available in consumer amounts. Together with the attractive broadband optical properties in the low THz range, where future communication systems will operate, makes this new twist on the classical tube waveguide very attractive.

Methods

Simulations. We carry out the numerical simulations on the lowest order fundamental core mode of the THz tubes transmission by using a commercially available FEM solver (COMSOL 3.5a). For the straight tube waveguide, we use the four-fold symmetry of the tube cross section to reduce the computational domain to one quarter using proper boundary conditions. This method allows one to model a waveguide using only one quarter of the mesh elements of the full structure. For the bent tube waveguide, the structure has two-fold symmetry. Perfect electric conductor or perfect magnetic conductor boundary conditions are used on the inner boundary of the tube for solving two polarizations fundamental mode.

Measurements. We perform transmission measurements of the PMMA tube waveguides using a commercial fiber-coupled THz-TDS system (Picometrix T-Ray 4000) with an effective spectral range 0.1–2.0 THz. The system generates single-cycle THz pulses with a duration of approximately 0.5 ps, and we record the transmitted signals within a time window of 320 ps by forming the average of 10.000 to 100.000 individual scans, each recorded within 10 ms (total acquisition time 100 to 1000 seconds). Subsequent Fourier analysis of the spectral content of the transmitted signals is then used to interpret the frequency-dependent behavior of the tubes.

The general measurement protocol is as follows. For the straight tubes, first we record the output signal of each tube type with a certain length (5 cm for tube 1 and 2, 10 cm for tube 3), and use these signals as reference signals. We then join the entrance facets of tubes to be characterized with the exit facets of the reference tubes in a coaxial (in-line) fashion, and confirm that the coupling loss between the tube segments is negligible for frequencies below 1 THz. The THz signals transmitted through the tubes are recorded by the THz detector, arranged and aligned so that the focal plane of the detector is at the exit facet of the tubes. Tube 1 with 30 cm length was used for the experimental bend-loss characterization. We use three tubes, each with total length of

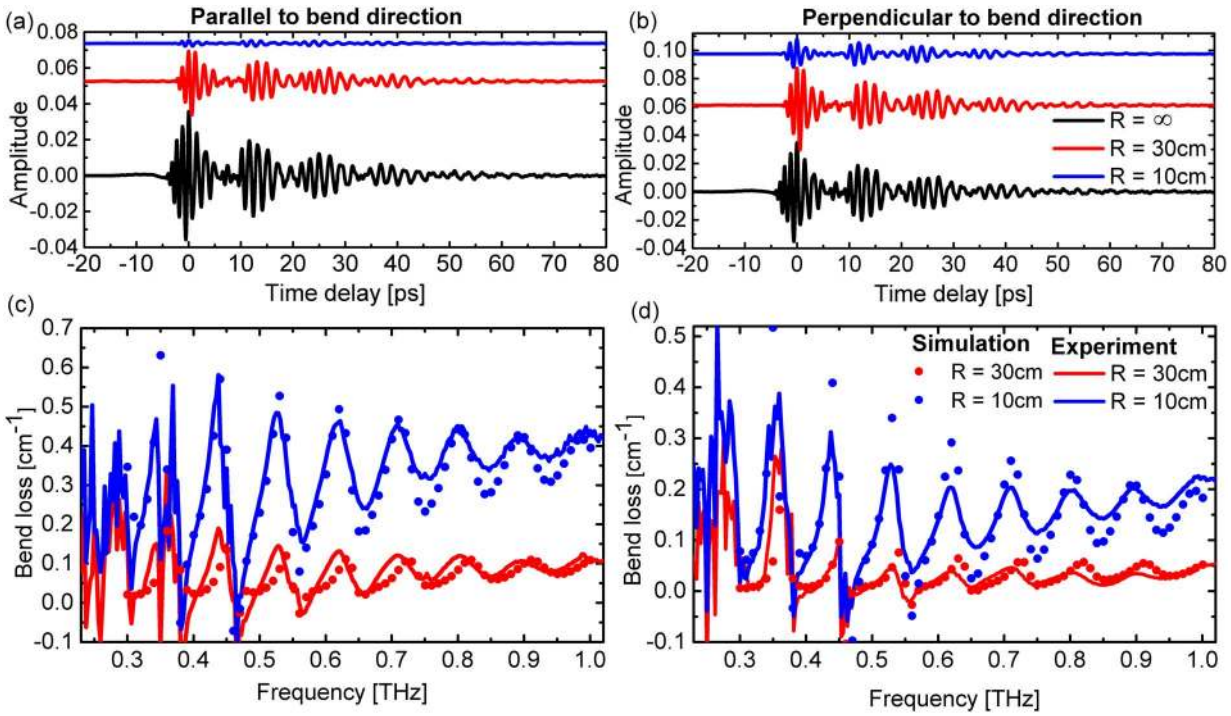

Figure 7 | (a) (b) Measured time-domain THz signals, and (c) (d) bend losses of 30 cm tube sample (ID = 4 mm, OD = 6.58 mm) with 18 cm bend length for different bending radii for two polarizations, parallel and perpendicular to the bend direction, with the simulated bend losses overlaid on the experimental values.

30 cm. One tube is straight and the other two are with the first and last 6 cm straight, but with a 18-cm long bendable section in the middle. Similar to the measurement method for straight tubes mentioned above, we again use the output from a 5 cm-long tube 1 as reference signal, and then joining the entrance facets of tubes to be measured with the exit facet of reference tube in a coaxial (in-line) connection. We measured the transmitted signal of a straight tube, and then the bent tubes with bend radii of 30 cm and 10 cm, respectively. In order to demonstrate the relation between bending loss and polarizations of input THz waves we performed the measurements at two different polarizations simply by rotating both emitter and receiver head (both linearly polarized) of the THz-TDS system by 90 degrees.

For the measurements of the effective index and GVD, due to a small uncertainty in the precise length of the fibers and the unavoidable phase ambiguity in THz-TDS when the phase varies rapidly, the measured phase data are corrected by multiples of 2π in a manner to ensure a continuous curve (except resonance frequencies) for the effective index without artificial jumps and we compensate the phase by numerically adjusting the distance from the exit facet to the detector by a small amount (typically < 1 mm) to make the experimental effective index as close as possible to the simulated index. This distance is impossible to maintain with micrometer precision between measurements on different tubes, and a small shift in position leads to a temporal shift of the received THz waveforms.

1. Jepsen, P. U., Cooke, D. G. & Koch, M. Terahertz spectroscopy and imaging–Modern techniques and applications. *Laser Photon. Rev.* **5**, 124–166 (2011).
2. Atakaramians, S., Afshar, V. S., Monro, T. M. & Abbott, D. Terahertz dielectric waveguides. *Adv. Opt. Photonics* **5**, 169–215 (2013).
3. Mendis, R. R. & Grischkowsky, D. THz Interconnect with Low Loss and Low Group Velocity Dispersion. *IEEE Microw. Wirel. Compon. Lett.* **11**, 444–446 (2001).
4. Mendis, R. & Mittleman, D. M. Comparison of the lowest-order transverse electric (TE1) and transverse-magnetic (TEM) modes of the parallel-plate waveguide for terahertz pulse application. *Opt. Express* **17**, 14839–14850 (2009).
5. Jeon, T.-I. & Grischkowsky, D. Direct Optoelectronic Generation and Detection of Subps Electrical Pulses on Sub-mm Coaxial Transmission Lines. *Appl. Phys. Lett.* **85**, 6092–6094 (2004).
6. Wang, K. & Mittleman, D. M. Metal wires for terahertz wave guiding. *Nature* **432**, 376–379 (2004).
7. Jeon, T. I., Zhang, J. & Grischkowsky, D. THz Sommerfeld wave propagation on a single metal wire. *Appl. Phys. Lett.* **86**, 161904 (2005).
8. Jo, J. S., Jeon, T.-I. & Grischkowsky, D. Prototype 250 GHz Bandwidth Chip to Chip Electrical Interconnect, Characterized with Ultrafast Optoelectronics. *IEEE Trans. Terahertz Sci. Technol.* **3**, 453–460 (2013).
9. Deibel, J. A., Wang, K., Escarra, M. D. & Mittleman, D. Enhanced coupling of terahertz radiation to cylindrical wire waveguides. *Opt. Express* **14**, 279–290 (2006).
10. Dai, J., Zhang, J., Zhang, W. & Grischkowsky, D. THz Time-Domain Spectroscopy (THz-TDS) Characterization of the Far-Infrared Absorption and Index of Refraction of High-Resistivity, Float-Zone Silicon. *J. Opt. Soc. Am. B.* **21**, 1379–1386 (2004).
11. Mbonye, M., Mendis, R. & Mittleman, D. M. A terahertz two-wire waveguide with low bending loss. *Appl. Phys. Lett.* **95**, 233506 (2009).
12. Bowden, B., Harrington, J. A. & Mitrofanov, O. Silver/polystyrene-coated hollow glass waveguides for the transmission of terahertz radiation. *Opt. Lett.* **32**, 2945–2947 (2007).
13. Navarro-Cía, M. *et al.* Terahertz wave transmission in flexible polystyrene-lined hollow metallic waveguides for the 2.5–5 THz band. *Opt. Express* **21**, 23748–23755 (2013).
14. Tang, X. L. *et al.* Elliptical hollow fiber with inner silver coating for linearly polarized terahertz transmission. *IEEE Photon. Technol. Lett.* **25**, 331–334 (2013).
15. Mendis, R. & Grischkowsky, D. Plastic ribbon THz waveguides. *J. Appl. Phys.* **88**, 4449–4451 (2000).
16. Nielsen, K. *et al.* Bendable, low-loss Topas fibers for the terahertz frequency range. *Opt. Express* **17**, 8592–8601 (2009).
17. Tuniz, A. *et al.* Metamaterial fibres for subdiffraction imaging and focusing at terahertz frequencies over optically long distances. *Nat. Commun.* **4** doi:10.1038/ncomms3706 (2013).
18. Han, H., Park, H., Cho, M. & Kim, J. Terahertz pulse propagation in a plastic photonic crystal fiber. *Appl. Phys. Lett.* **80**, 2634–2636 (2002).
19. Anthony, J., Leonhardt, R., Argyros, A. & Large, M. C. Characterization of a microstructured Zeonex terahertz fiber. *J. Opt. Soc. Am. B* **28**, 1013–1018 (2011).
20. Ung, B., Mazhorova, A., Dupuis, A., Rozé, M. & Skorobogatiy, M. Polymer microstructured optical fibers for terahertz wave guiding. *Opt. Express* **19**, 848–861 (2011).
21. Chen, L. J., Chen, H. W., Kao, T. F., Lu, J. Y. & Sun, C. K. Low-loss subwavelength plastic fiber for terahertz waveguiding. *Opt. Lett.* **31**, 308–310 (2006).
22. Rozé, M., Ung, B., Mazhorova, A., Walther, M. & Skorobogatiy, M. Suspended core subwavelength fibers: towards practical designs for low-loss terahertz guidance. *Opt. Express* **19**, 9127–9138 (2011).
23. Hassani, A., Dupuis, A. & Skorobogatiy, M. Porous polymer fibers for low-loss Terahertz guiding. *Opt. Express* **16**, 6340–6351 (2008).
24. Hassani, A., Dupuis, A. & Skorobogatiy, M. Low loss porous terahertz fibers containing multiple subwavelength holes. *Appl. Phys. Lett.* **92**, 071101 (2008).
25. Atakaramians, S. *et al.* THz porous fibers: design, fabrication and experimental characterization. *Opt. Express* **17**, 14053–15062 (2009).
26. Atakaramians, S. *et al.* Direct probing of evanescent field for characterization of porous terahertz fibers. *Appl. Phys. Lett.* **98**, 121104 (2011).
27. Ponseca Jr, C. S. *et al.* Transmission of terahertz radiation using a microstructured polymer optical fiber. *Opt. Lett.* **33**, 902–904 (2008).
28. Wu, Z., Ng, W. R., Gehm, M. E. & Xin, H. Terahertz electromagnetic crystal waveguide fabricated by polymer jetting rapid prototyping. *Opt. Express* **19**, 3962–3972 (2011).
29. Dupuis, A., Stoeffler, K., Ung, B., Dubois, C. & Skorobogatiy, M. Transmission measurements of hollow-core THz Bragg fibers. *J. Opt. Soc. Am. B* **28**, 896–907 (2011).
30. Ung, B., Dupuis, A., Stoeffler, K., Dubois, C. & Skorobogatiy, M. High-refractive-index composite materials for terahertz waveguides: trade-off between index contrast and absorption loss. *J. Opt. Soc. Am. B* **28**, 917–921 (2011).
31. Nielsen, K., Rasmussen, H. K., Jepsen, P. U. & Bang, O. Porous-core honeycomb bandgap THz fiber. *Opt. Lett.* **36**, 666–668 (2011).
32. Bao, H., Nielsen, K., Rasmussen, H. K., Jepsen, P. U. & Bang, O. Fabrication and characterization of porous-core honeycomb bandgap THz fibers. *Opt. Express* **20**, 29507–29517 (2012).
33. Anthony, J., Leonhardt, R., Leon-Saval, S. G. & Argyros, A. THz propagation in Kagome hollow-core microstructured fibers. *Opt. Express* **19**, 18470–18478 (2011).
34. Vincetti, L. & Setti, V. Extra loss due to Fano resonances in inhibited coupling fibers based on a lattice of tubes. *Opt. Express* **20**, 14350–14361 (2012).
35. Setti, V., Vincetti, L. & Argyros, A. Flexible tube lattice fibers for terahertz applications. *Opt. Express* **21**, 3388–3399 (2013).
36. Lai, C. H. *et al.* Low-index terahertz pipe waveguides. *Opt. Lett.* **34**, 3457–3459 (2009).
37. Lai, C. H. *et al.* Modal characteristics of antiresonant reflecting pipe waveguides for terahertz waveguiding. *Opt. Express* **18**, 309–322 (2010).
38. Lu, J. T., Hsueh, Y. C., Huang, Y. R., Hwang, Y. J. & Sun, C. K. Bending loss of terahertz pipe waveguides. *Opt. Express* **18**, 26332–26338 (2010).
39. Lai, C. H., Chang, T. & Yeh, Y. S. Characteristics of bent terahertz antiresonant reflecting pipe waveguides. *Optics express* **22**, 8460–8472 (2014).
40. Nguema, E., Férachou, D., Humbert, G., Auguste, J. L. & Blondy, J. M. Broadband terahertz transmission within the air channel of thin-wall pipe. *Opt. Lett.* **36**, 1782–1784 (2011).
41. Lu, J. Y. *et al.* Terahertz air-core microstructure fiber. *Appl. Phys. Lett.* **92**, 064105 (2008).
42. Harrington, J. A., George, R., Pedersen, P. & Mueller, E. Hollow polycarbonate waveguides with inner Cu coatings for delivery of terahertz radiation. *Opt. Express* **12**, 5263–5268 (2004).
43. Mitrofanov, O., James, R., Fernández, F. A., Mavrogordatos, T. K. & Harrington, J. A. Reducing transmission losses in hollow THz waveguides. *IEEE Trans. Terahertz Sci. Technol.* **1**, 124–132 (2011).
44. Litchinitser, N. M., Abeeluck, A. K., Headley, C. & Eggleton, B. J. Antiresonant reflecting photonic crystal optical waveguides. *Opt. Lett.* **27**, 1592–1594 (2002).
45. Zhou, S. F. *et al.* Characterization and modeling of Bragg gratings written in polymer fiber for use as filters in the THz region. *Opt. Express* **20**, 9564–9571 (2012).
46. Yan, G. *et al.* Resonant THz sensor for paper quality monitoring using THz fiber Bragg gratings. *Opt. Lett.* **38**, 2200–2202 (2013).
47. Yan, G. *et al.* Low-loss terahertz waveguide Bragg grating using a two-wire waveguide and a paper grating. *Opt. Express* **16**, 3089–3092 (2013).
48. Bao, H., Nielsen, K., Rasmussen, H. K., Jepsen, P. U. & Bang, O. Design and optimization of mechanically down-doped terahertz fiber directional couplers. *Opt. Express* **22**, 9486–9497 (2014).
49. Nielsen, K., Rasmussen, H. K., Jepsen, P. U. & Bang, O. Broadband terahertz fiber directional coupler. *Opt. Lett.* **35**, 2879–2881 (2010).
50. Chen, H. W. *et al.* Subwavelength dielectric-fiber-based THz coupler. *J. Lightwave Technol.* **27**, 1489–1495 (2009).
51. Dupuis, A. *et al.* Fabrication and THz loss measurements of porous subwavelength fibers using a directional coupler method. *Opt. Express* **17**, 8012–8028 (2009).
52. Lu, J. T. *et al.* Terahertz pipe-waveguide-based directional couplers. *Opt. Express* **19**, 26883–26890 (2011).
53. Lai, C. H., Sun, C. K. & Chang, H. C. Terahertz antiresonant-reflecting-hollow-waveguide-based directional coupler operating at antiresonant frequencies. *Opt. Lett.* **36**, 3590–3592 (2011).
54. Jördens, C. *et al.* Dielectric fibres for low-loss transmission of millimetre waves and its application in couplers and splitters. *J. Infrared Millim. Terahertz Waves* **31**, 214–220 (2010).
55. Li, S. *et al.* Terahertz polarization splitter based on orthogonal microstructure dual-core photonic crystal fiber. *Appl. Opt.* **52**, 3305–3310 (2013).
56. Marcatili, E. A. J. & Schmeltzer, R. A. Hollow metallic and dielectric waveguides for long distance optical transmission and lasers. *The Bell System Technical Journal* **43**, 1783–1809 (1964).
57. Jepsen, P. U. & Fischer, B. M. Dynamic range in terahertz time-domain transmission and reflection spectroscopy. *Opt. Lett.* **30**, 29–31 (2005).
58. Thrane, L., Jacobsen, R. H., Jepsen, P. U. & Keiding, S. R. THz reflection spectroscopy of liquid water. *Chem. Phys. Lett.* **240**, 330–333 (1995).

59. Møller, U., Cooke, D. G., Tanaka, K. & Jepsen, P. U. Terahertz reflection spectroscopy of Debye relaxation in polar liquids [Invited]. *J. Opt. Soc. Am. B* **26**, A113–A125 (2009).
60. Heiblum, M. & Harris, J. Analysis of curved optical waveguides by conformal transformation. *IEEE J. Quantum Electron.* **11**, 75–83 (1975).

Acknowledgments

This work was financial supported by the Danish Council for Independent Research (FTP Project HI-TERA).

Author contributions

P.U.J. supervised the experiments and O.B. supervised the simulations. H.B. performed the simulations and experiments. H.B., K.N., O.B. and P.U.J. performed the data analysis, wrote and reviewed the manuscript.

Additional information

Competing financial interests: The authors declare no competing financial interests.

How to cite this article: Bao, H., Nielsen, K., Bang, O. & Jepsen, P.U. Dielectric tube waveguides with absorptive cladding for broadband, low-dispersion and low loss THz guiding. *Sci. Rep.* **5**, 7620; DOI:10.1038/srep07620 (2015).